

Phase Diagram of Triangular Lattice Quantum Ising Model under External Field

Yuan Da Liao,^{1,2,*} Han Li,^{3,*} Zheng Yan,^{4,5} Hao-Tian Wei,^{5,6} Wei Li,^{3,7,†} Yang Qi,^{5,6,‡} and Zi Yang Meng^{4,§}

¹*Beijing National Laboratory for Condensed Matter Physics and Institute of Physics,
Chinese Academy of Sciences, Beijing 100190, China*

²*School of Physical Sciences, University of Chinese Academy of Sciences, Beijing 100190, China*

³*School of Physics, Beihang University, Beijing 100191, China*

⁴*Department of Physics and HKU-UCAS Joint Institute of Theoretical and Computational Physics,
The University of Hong Kong, Pokfulam Road, Hong Kong SAR, China*

⁵*State Key Laboratory of Surface Physics, Fudan University, Shanghai 200438, China*

⁶*Center for Field Theory and Particle Physics, Department of Physics, Fudan University, Shanghai 200433, China*

⁷*International Research Institute of Multidisciplinary Science, Beihang University, Beijing 100191, China*

(Dated: March 17, 2021)

Quantum Ising model on a triangular lattice hosts a finite temperature Berezinskii-Kosterlitz-Thouless (BKT) phase with emergent U(1) symmetry, and it will transit into an up-up-down (UUD) phase with C_3 symmetry breaking upon an infinitesimal external field along the longitudinal direction, but the overall phase diagram spanned by the axes of external field and temperature remains opaque due to the lack of systematic investigations with controlled methodologies. By means of quantum Monte Carlo at finite temperature and ground state density matrix renormalization group simulations, we map out the phase diagram of triangular quantum Ising model. Starting from the upper BKT temperature at zero field, we obtain the phase boundary between the UUD and paramagnetic phases with its 2D $q = 3$ Potts universality at weak field and weakly first order transition at strong field. Originated from the lower BKT temperature at zero field, we analyze the low temperature phase boundary between the clock phase and the UUD phase with Ising symmetry breaking at weak fields and the quantum phase transition between the UUD and fully polarized phases at strong fields. The accurate many-body numerical results are consistent with our field theoretical analysis. The experimental relevance towards the BKT magnet TmMgGaO₄ and programmable quantum simulators are also discussed.

I. INTRODUCTION

Frustrated magnets can host intriguing quantum many-body states and phenomena that trigger great research interest recently. For example, the rare-earth compound TmMgGaO₄ (TMGO) [1–4] is revealed to realize a triangular lattice quantum Ising (TLI) model exhibiting the Berezinskii-Kosterlitz-Thouless (BKT) phase transitions [4–6]. The Ising spins in the TLI model cooperate in the way such that there emerges an U(1) symmetry at finite temperature in the BKT phase, with power-law spin correlation and separating the low- T clock ordered and high- T paramagnetic phases with two BKT phase transitions [5, 7–9].

Recently, measurements have been performed to explore the BKT physics in this materials [4, 10]. In particular, the nuclear magnetic resonance (NMR) probe found an extended regime with strong fluctuations that is consistent with an intermediate BKT phase [4], and the inelastic neutron scattering (INS) detection also suggest the existence of vortex characteristics at finite temperature [10]. Under external fields h , there is also strong interest and experimental progress on the thermodynamics and dynamical properties of the material [6, 11, 12], which raised questions and inspire theoretical effort to understand the h - T phase diagram of the TLI model. Despite some initial efforts, there remains open questions on the nature

of field-induced ordered phases and the universality class of phase transitions between such ordered and the paramagnetic phase above the upper BKT temperature and the clock ordered phase below, which are very relevant for the understanding of TMGO experiments.

In this work, we combine multiple quantum many-body theoretical tools, including finite-temperature quantum Monte Carlo (QMC), ground-state density matrix renormalization group (DMRG) and field-theoretical renormalization group (RG) analysis, to perform an unbiased study of the TLI model under the longitudinal fields. At the ground state, we found two field-induced quantum phase transitions (QPTs) that a lower-field Ising QPT (at h_{c1}) separating the clock and up-up-down (UUD) phases and a weakly first-order QPT (at h_{c2}) between the UUD and polarized phases. We also studied the finite-temperature fate of these two QPTs: The lower QPT field h_{c1} reduces as T increases, and the thermal phase transition of 2D Ising type is continuously connected to the lower BKT transition at zero field; on the other hand, the first-order QPT at h_{c2} also persists at finite T , with transition field also reduces as T increases and turns into a continuous thermal phase transition of 2D $q = 3$ Potts universality through a tricritical point, and eventually connects to the higher BKT transition at zero field (cf. the phase diagram in Fig. 1 (b)), unified with the previous understanding of the zero-field phase diagram of the TLI model [5, 8, 9]. Such a phase diagram is also consistent with the experimental observations at hand and can be used to guide future ones.

* These two authors contributed equally

† w.li@buaa.edu.cn

‡ qiyang@fudan.edu.cn

§ zymeng@hku.hk

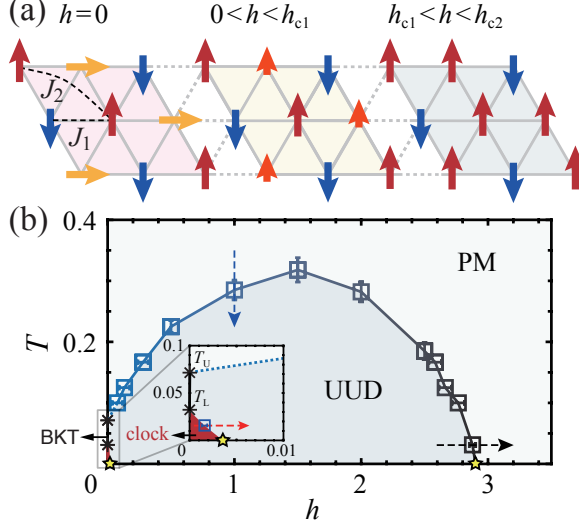


FIG. 1. (a) Phases at low temperature, starting from the clock phase at zero external magnetic field (left) to the slightly polarized clock phase at weak field (middle), and the UUD phase under intermediate field (right). The spin-up and spin-down arrows are all along the external longitudinal field h and the superposition $|\rightarrow\rangle$ is along the intrinsic transverse field Δ . (b) The h - T phase diagram of the model in Eq. (1) with $J_1 = 1$, $J_2 = 0$ and $\Delta = 0.2$. The two asterisks (*) at T_U and T_L along the T -axis stand for the upper and lower BKT temperatures of the model at $h = 0$. The blue phase boundary is the continuous phase transition with 2D $q = 3$ Potts universality starting from the T_U , which separates the PM from the UUD phases; the black phase boundary is the weakly first-order transition line separating the same two phases. Inset zooms in at small h and T with the BKT phase at $h = 0$ as well as the clock phase (red area) and its Ising transition to the UUD phase depicted. The Ising transition originates from the T_L at $h = 0$. The precise position of the phase boundaries are obtained from QMC (open squares) and DMRG (yellow stars), and the shape of the phase diagram is consistent with the RG analysis (see discussions in Appendices C). The red, blue, and black dashed arrows indicate the representative parameter paths used in Figs. 2 and 3, respectively.

II. MODEL, METHODS, AND ORDER PARAMETER

We study the TLI model under the external longitudinal field as

$$H = J_1 \sum_{\langle i,j \rangle} S_i^z S_j^z + J_2 \sum_{\langle\langle i,j \rangle\rangle} S_i^z S_j^z - \sum_i (\Delta S_i^x + h S_i^z), \quad (1)$$

where $J_1 = 1$ is the nearest-neighbor antiferromagnetic interaction and set as the energy unit, and J_2 represents a small next-nearest neighbor interaction. Although setting $J_2 = 0$ in this work, we note that the small J_2 in the model and material could trigger interesting incommensurate phase and string magnetic excitations as discussed in Refs. [13, 14]. $\Delta = 0.2$ represents the intrinsic transverse field in the material and h represents the external magnetic field along longitudinal direction. Fig. 1(a) is the sketch of the 2D triangular lattice, with the J_1, J_2 interactions and the spin orientation from the clock phase (left, $h = 0$) to the slightly polarized clock phase at intermediate field (middle, $0 < h < h_{c1}$), and the UUD

phase (right, $h_{c1} < h < h_{c2}$). The obtained phase diagram is shown in Fig. 1(b), where the rich phases and transitions will be discussed below.

To solve the model in an unbiased manner, we implement the stochastic series expansion QMC method [15–18] to simulate the model on finite lattice sizes and temperatures (with the linear system size L up to 21 and T down to 1/64), and by means of the finite size analysis, map out the finite-temperature phase diagram and distinguish the different phase transitions. The ground state properties are computed with DMRG on a cylindrical geometry of size $YC W \times L$ with W up to 12 and L to 45. The retained states are up to $D = 1024$, with truncation errors $\epsilon \lesssim 10^{-7}$ guaranteeing the convergence of the DMRG calculations. The phase diagram has also been analyzed with RG in qualitative manner. Details of the numerical and field-theoretical implementations are given in Appendices C and D.

The TLI model without external field has been thoroughly studied [5, 7–9]. As shown in Fig. 1(b), along the T -axis, starting from the paramagnetic phase (PM) the system will first enter a BKT phase with emergent U(1) symmetry and power-law spin correlations and then turn into a clock phase at lower temperature. The upper and lower BKT temperatures are denoted as the asterisks (*) in Fig. 1(b). The clock phase (and the UUD phase under external field) can be conveniently detected by the following complex order parameter [8, 9], $me^{i\theta} \equiv (m_1 + m_2 e^{i(4\pi/3)} + m_3 e^{i(-4\pi/3)})/\sqrt{3}$, where the m_i with $i = 1, 2, 3$ represent the magnetization of the three sublattices; m and θ represent the magnitude and the phase of the complex order parameter. $me^{i\theta}$ exhibits an emergent U(1) symmetry in the BKT phase, and falls into one of six minima at $(2n-1)\frac{\pi}{6}$ in the clock phase, with $n = 1, 2, \dots, 6$ [cf. the red dots in Fig. 2(f)].

When an external field h is applied, the model develops an UUD phase. RG analysis in Appendices C shows that h is a relevant perturbation in the BKT phase, leading to the UUD phase at infinitesimal field. However, above and below the BKT temperature range, the PM and clock phases are both gapped, and thus stable under an infinitesimal field. Therefore, it is expected that the phase boundaries between the UUD phase and the PM/clock phases appear at finite h , extrapolating to zero field at the upper(lower) temperature of the BKT phase, respectively.

The universality class of the phase transitions can be understood as follows. The UUD phase can also be represented by the complex order parameter $me^{i\theta}$ with θ taking one of three minima at π and $\pm\pi/3$ [the green dots in Fig. 2(f)]. On the other hand, the clock phase, in the presence of h , still has six minima. However, their locations move to $(2n-1)\frac{\pi}{6} + (-1)^{n-1}\delta$, where δ is an h -dependent angle, as indicated by the arrows in Fig. 2(f). When $\delta = 0$, the minima are evenly distributed around a circle in the complex plane, which represent the clock state at $h = 0$ [9]. When $\delta = \frac{\pi}{6}$, they become the three minima of the UUD phase, and the state of UUD phase will spontaneously break this discrete C_3 symmetry.

It is interesting to see that such symmetry analysis can be verified by QMC simulation. As shown in Fig. 2(a)–(e), we plot the histograms of the complex order parameter $me^{i\theta}$ at

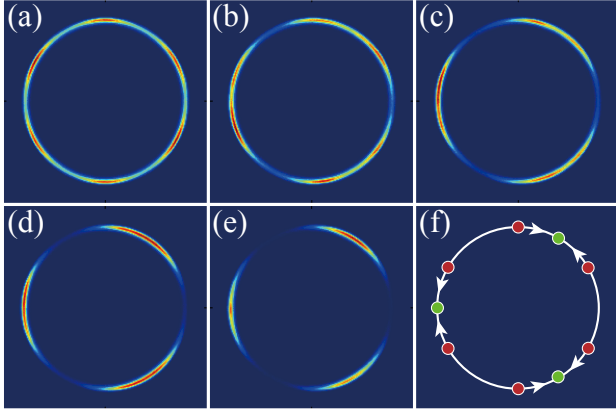


FIG. 2. (a)-(e) Histogram of $me^{i\theta}$ from $h = 0$ to $h = 0.01$ with interval $\Delta h = 0.0025$. In QMC simulations, the temperature is $T = 1/64$ and the system size is $L = 9$, the parameter path is from the clock phase to the UUD phase indicated by the red dashed arrow in the inset of Fig. 1(b). (f) The six red points represent the locations of six minima of complex order parameter in clock phase. The three green points represent the locations of three minima of complex order parameter in UUD phase. Their movements (indicated by the white arrows) are shown in (a) - (e) with real QMC data.

different h [starting from $h = 0$ and increasing with footstep $\Delta h = 0.0025$ to $h = 0.01$, the path is shown by the red dashed arrow in the inset of Fig. 1(b)] at low temperature $T = 1/64$ with system size $L = 9$. The positions of bright spots represent the locations of minima, and they move as expected. Fig. 2(f) shows the locations of minima of $me^{i\theta}$ in theoretical symmetry analysis and the white arrows indicate the movement of the bright spots. The finite (but low) temperature continuous transition between the clock and the UUD phases therefore belongs to the 2D Ising universal class, as each green dot minimum of θ further splits into two red ones. On the other hand, the continuous transition from the PM to the UUD phases, as we will discuss below, belongs to the 2D $q = 3$ Potts universal class, as θ falls into one of the three green dot minima. Physically, the transitions at these two phase boundaries break the three-fold rotation and mirror reflection symmetries of the lattice, respectively.

III. PHASE DIAGRAM

Our phase diagram is shown in Fig. 1(b), the PM, UUD, BKT and clock phases are in place. Our numerical results reveal that the UUD-PM phase transition is continuous and belongs to the 2D $q = 3$ Potts universality at weak field ($h < 1.5$) and becomes weakly first order at strong field ($h > 1.5$) [19, 20] (see Appendices B for details). The boundary of UUD phase extrapolates to the upper BKT temperature at $h = 0$.

To study the UUD-PM phase transition and its finite size scaling in QMC, we employ the Binder cumulant for the q -state Potts phase transition, $U(q) = \frac{q+1}{2}(1 - \frac{q-1}{q+1} \frac{\langle m^4 \rangle}{\langle m^2 \rangle^2})$, where m is the order parameter, $\langle \rangle$ means the statistical average in QMC.

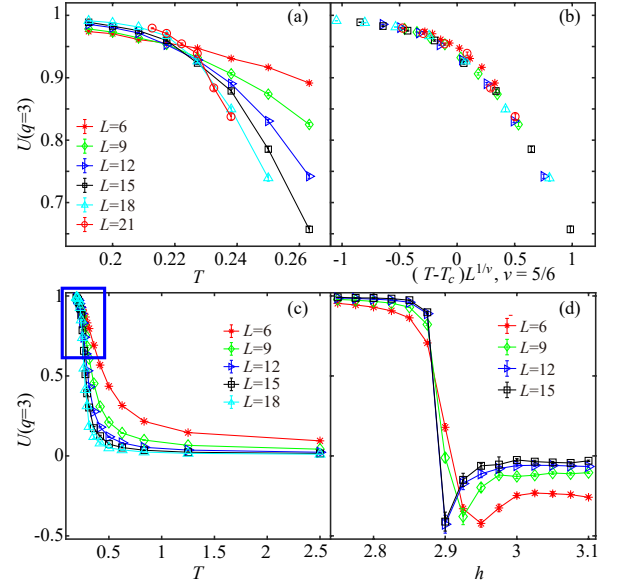


FIG. 3. (a) shows the Binder cumulant $U(q)$ of the 2D $q = 3$ Potts transition. At $h = 0.5$ and the temperature reduces from the PM to UUD phases. The cross of U for different system sizes indicate the continuous phase transition point between PM at high temperature and UUD phase at low temperature, with $T_c = 0.23(2)$. In (b), we perform the data collapse of Binder cumulant with 2D $q = 3$ Potts critical exponent $v = 5/6$ as $(T - T_c)L^{1/v}$ close to T_c . (c) shows the wider temperature range of the Binder cumulant compared with the zoom-in in (a) – denoted as the blue rectangle box. U varies continuously from 0 at high temperature to 1 at low temperature. The nature of this continuous transition is revealed in (a) and (b). In (d), along the path of black dashed arrow in Fig. 1(b), the transition from the UUD phase to the polarized PM phase is weakly first-order, as indicated by the negative dip in the U .

For a continuous transition, U extrapolates to the saturation value 1 when $T < T_c$, and decays to 0 at high temperature when $T > T_c$, and curves of different sizes cross at T_c [21, 22]. This is what we saw in the Fig. 3(a) and (c), in which the QMC results of $U(q = 3)$ along the path of blue dashed arrow in Fig. 1(b) are shown. Fig. 3(c) is the overall scale with a wide temperature range and we note that $U(q = 3)$ indeed reduce from 1 to 0 as temperature increases. Fig. 3(a) is a zoom-in in the critical region (as denoted by the blue rectangle in Fig. 3(c)), here U crosses at a critical point for different L and one can readily read $T_c = 0.23(2)$. We further collapse U with the 2D $q = 3$ Potts exponent $v = 5/6$ according to the scaling relation $U(q) = f((T - T_c)L^{1/v})$, and the results are shown in Fig. 3(b). This good data collapse evidence that UUD-PM transition is continuous and indeed belongs to the $q = 3$ Potts universality. The other blue square phase boundary points in Fig. 1(b) are determined in similar manner.

At large h , the transition between UUD and PM becomes weakly first order, and this can also be seen from the Binder cumulant [23]. As shown in Fig. 3(c) and (d), we make a comparison between the Potts transition and the first order transition, along the two different parameter paths indicated by the blue and black dashed arrows in Fig. 1(b). In Fig. 3(c)

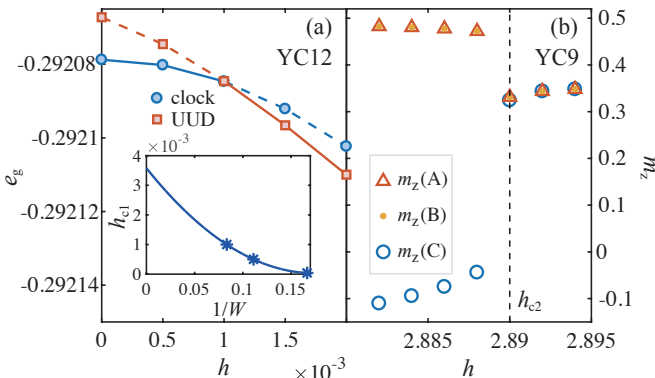


FIG. 4. (a) The bulk energy curves e_g calculated by DMRG on the $YC12 \times 30$ cylinder under different (clock and UUD) boundary pinning fields exhibit a crossing at $h_{c1} \simeq 0.001$. In the inset, the crossing fields h_{c1} calculated under system width $W = 6, 9$ and 12 are extrapolated to $1/W \rightarrow 0$, from which we determine $h_{c1} \simeq 0.0036$ as the transition point between the two phases. (b) The QPT near the upper critical field $h_{c2} \simeq 2.89$. The magnetization m_z results provide clearly evidences of a three-sublattice UUD order for $h < h_{c2}$, while m_z becomes uniform in the polarized phase for $h > h_{c2}$. The data are from DMRG calculations on a $YC9 \times 45$ cylinder.

the continuous 2D Potts transition is shown, and one sees that the U changes continuously and always above zero, and the different curves cross at the $T_c = 0.23(2)$ (as shown in Fig. 3(a)). The contrast is very obvious in Fig. 3(d). Here we fix the temperature at $T = 1/32$ and scan the field h . It is clear that close to the UUD to PM (here means polarized phase) transition, the U develops a negative dip at the transition point, this is the signature of a first-order phase transition, where the system in the Monte Carlo simulations can be either inside the ordered phase or inside the disordered phase [23]. And when the $h > 2.9$, the system enters the PM phase. We note that the transition is actually of weakly first order, as the U didn't diverge at the present L , this is also consistent with the experiment in $TmMgGaO_4$ with the magnetic excitation gap observed to be very small near the high transition field [11].

With the high field phase boundary between the UUD and PM determined, we now look for the low field ones between the clock phase and the UUD phase, as indicated in the inset of Fig. 1(b). The RG calculation in Appendices C predicted the shape of the phase boundary boundary and find it lies very close to the vertical T axis with $h = 0$ (see Fig. S3), and our numerical result is consistent with such prediction. The symmetry analysis reveals that this is an Ising transition since the clock and UUD phases differs by a Z_2 symmetry (cf. Fig. 2). Since the temperature here turns out to be too low to have large-scale QMC simulations, we turn to DMRG computation directly at $T = 0$.

IV. DMRG STUDY OF THE GROUND-STATE PHASE DIAGRAM

DMRG calculations are employed to compute the ground-state phase diagram. In Fig. 4, we show the numerical evidence of two QPTs at lower (h_{c1}) and higher (h_{c2}) critical fields, respectively. In the calculations, we introduce two kinds of pinning fields on the outmost two columns of the cylindrical system, which respectively favor the clock and UUD order, and compute the observables in the bulk (see Appendices D). Such pinning fields, although applied only on the boundary of the system, can nevertheless stabilize the two types of ordered states in the bulk, and can be used to discern the subtle competition between different quantum states at low magnetic fields.

In Fig. 4(a), we plot the bulk energy measured in the very center of the long cylinder, and see that the clock phase is energetically more favorable at lower fields, while the UUD phase takes the place as the true ground state at higher fields, with the crossing point at $h_{c1} \simeq 0.001$ (for width $W = 12$), which could be extrapolated to 0.0036 for $1/W \rightarrow 0$, as shown in the inset of Fig. 4(a). As the field further increases, the UUD order would also get suppressed, and a phase transition to polarized phase takes place at around $h_{c2} \simeq 2.89$. As shown in Fig. 4(b), the local magnetization in the UUD phase, $m_z(A) = m_z(B) \neq m_z(C)$ on the three sublattices A, B, and C, becomes uniform $m_z(A) = m_z(B) = m_z(C)$ in the polarized phase. The obtained ground state h_{c1} and h_{c2} are denoted as the yellow stars in the phase diagram of Fig. 1(b), and are well connected with the finite temperature phase boundaries of QMC.

V. EXPERIMENTAL RELEVANCE

Our results have immediate connections to experiments on the rare-earth compound $TmMgGaO_4$ [1–5], where the existence of BKT transitions and an intermediate floating phase has been theoretically proposed [5] and experimentally detected in NMR [4]. There is currently upsurging research interest on further experimental exploration of the BKT physics [10], and the field-tunable quantum states in the compound [11]. Our results, combining finite-temperature QMC and ground-state DMRG calculations, unambiguously pinpoint the two quantum phase transitions, at the lower- h_{c1} (clock to UUD) and upper-field h_{c2} (UUD to polarized). Although the model parameters in this work are simplified [5], we can still resolve the two QPTs and the upper field h_{c2} is very close to 3.7 T when taking $J_1 = 1$ meV, in good agreement to experiments [2–4].

Moreover, we show numerical evidence from large-scale QMC calculations that there exist a continuous thermal phase transition that belongs to the 3-state Potts universality class, under finite external fields. Such Potts transition gradually changes into a weakly first-order phase transition around h_{c2} . These theoretical predictions can be confirmed in future thermodynamic and dynamical measurements of the material, which should exhibit universal scaling near the transition point.

Our model could also be implemented and further detected in the programmable quantum simulators based on Rydberg atom arrays [24–26] and superconducting qubits [27, 28] where geometry frustration and quantum dynamics of quantum Ising models have been proposed and partially realized.

ACKNOWLEDGMENTS

We thank Weiqiang Yu, Jinsheng Wen for valuable discussions. YDL, ZY and ZYM acknowledge support from the RGC of Hong Kong SAR of China (Grant Nos. 17303019 and 17301420), MOST through the National Key Research and Development Program (Grant No. 2016YFA0300502) and the Strategic Priority Research Program of the Chinese Academy of Sciences (Grant No. XDB33000000). HL and WL acknowledge the support from the National Natural Science Foundation of China (Grant Nos. 11834014 and 11974036). HTW and QY acknowledge supports from MOST under Grant No. 2015CB921700 and from NSFC under Grant No. 11874115. We thank the Center for Quantum Simulation Sciences in the Institute of Physics, Chinese Academy of Sciences, the Computational Initiative at the Faculty of Science and the Information Technology Services at the University of Hong Kong and the Tianhe-1A Tianhe-2 and Tianhe3 prototype platforms at the National Supercomputer Centers in Tianjin and Guangzhou for their technical support and generous allocation of CPU time.

Appendix A: SSE-QMC Method

In this section, we describe the implementation of SSE-QMC algorithm of the quantum Ising model [16–18].

1. SSE on σ^z Basis

The Hamiltonian for our model is $H = J_1 \sum_{\langle i,j \rangle} S_i^z S_j^z + J_2 \sum_{\langle\langle i,j \rangle\rangle} S_i^z S_j^z - \sum_i (\Delta S_i^x + h S_i^z)$, we can decompose this Hamiltonian into diagonal or off-diagonal site and bond operators

$$\begin{aligned} H_{0,0} &= I \\ H_{-1,i} &= \frac{\Delta}{2} (S_i^+ + S_i^-) \\ H_{0,i} &= h_0 + h S_i^z \\ H_{1,b} &= J_1 \left(\frac{1}{4} - S_{b(1)}^z S_{b(2)}^z \right) \\ H_{1,b'} &= J_2 \left(\frac{1}{4} - S_{b'(1)}^z S_{b'(2)}^z \right) \end{aligned} \quad (A1)$$

with $H = - \sum_i (H_{-1,i} + H_{0,i}) - \sum_{b,b'} (H_{1,b} + H_{1,b'})$, noting we add some constants into it which doesn't change the physics. Here b (b') means the NN (NNN) bond, $H_{0,0}$ denotes the identity operator, $H_{-1,i}$ ($H_{0,i}$) denotes the off-diagonal (diagonal) operator on site i , $H_{1,b}$ ($H_{1,b'}$) denotes the diagonal operator on bond b (b'). $b(1)$ ($b'(1)$) and $b(2)$ ($b'(2)$) represent

the two sites connecting the bond b (b'). $S_i^+ = S_i^x + i S_i^y$ and $S_i^- = S_i^x - i S_i^y$ represent the creation and destruction operator of spin-1/2. In order to make these site and bond operators positive, we add $\frac{1}{4}$ in $H_{1,b}$ ($H_{1,b'}$) and have to set the constant $h_0 \geq h/2$.

It is well known that the partition function $Z = \text{Tr } e^{-\beta H}$ can be expressed as a power series expansion:

$$Z = \sum_{\alpha} \sum_{S_M} \frac{\beta^n (M-n)!}{M!} \left\langle \alpha \left| \prod_{i=1}^M H_{a_i, p_i} \right| \alpha \right\rangle, \quad (A2)$$

where β is the inverse of temperature, and M is the truncation of the expansion series n . Taking S^z as a complete set of basis for the system, the non-zero matrix elements for site operators and bond operators are

$$\begin{aligned} \langle \uparrow | H_{-1,i} | \downarrow \rangle &= \langle \downarrow | H_{-1,i} | \uparrow \rangle = \frac{\Delta}{2} \\ \langle \uparrow | H_{0,i} | \uparrow \rangle &= h_0 + \frac{h}{2} \\ \langle \downarrow | H_{0,i} | \downarrow \rangle &= h_0 - \frac{h}{2} \\ \langle \downarrow \uparrow | H_{1,b} | \downarrow \uparrow \rangle &= \langle \uparrow \downarrow | H_{1,b} | \uparrow \downarrow \rangle = \frac{J_1}{2} \\ \langle \downarrow \uparrow | H_{1,b'} | \downarrow \uparrow \rangle &= \langle \uparrow \downarrow | H_{1,b'} | \uparrow \downarrow \rangle = \frac{J_2}{2} \end{aligned} \quad (A3)$$

The updating scheme includes the diagonal update which either inserts or removes a diagonal operator between two states with probabilities regulated by the detailed balanced condition, and the cluster update which flips all the spins as following scheme. The configurations of the updating scheme are shown in Fig. 5.

We describe the updating scheme in the following steps:

1. Diagonal update

We go through the operator strings and either remove or insert a diagonal operator according to the following procedures.

- For a null operator ($H_{0,0}$), we substitute it with a diagonal operator $H_{0,i}$ $H_{1,b}$ or $H_{0,b'}$ by the procedures below. Firstly we make the decision of which position for diagonal operators to insert with a probability $1/(N+N_b+N_{b'})$, where N means the number of total sites, N_b ($N_{b'}$) means the number of total NN (NNN) bonds. If the chosen bond to insert a bond operator has an anti-parallel configurations, then the insertion of a bond operator at this place is prohibited. After the decision is made, accept the insertion of an operator with probability

$$P = \min \left(\frac{\beta(N+N_b+N_{b'}) \langle H_a \rangle}{M-n}, 1 \right), \quad (A4)$$

The H_a means $H_{0,i}$ $H_{1,b}$ or $H_{0,b'}$ which depends on the position we chosen.

- For a diagonal operator H_a , we removed it with probability,

$$P = \min \left(\frac{M-n+1}{\beta(N+N_b+N_{b'}) \langle H_a \rangle}, 1 \right) \quad (A5)$$

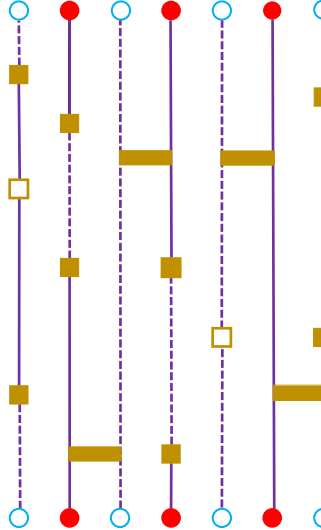


FIG. 5. SSE-QMC configuration of quantum Ising model. Golden bars represent Ising bond operators. Filled squares plaquette are off-diagonal site operators, and open plaquettes denote the diagonal site operators. Arrows represent periodic boundary conditions in the imaginary time direction. The red solid circles and the light blue open circles indicate spin up and down. Solid and dashed purple lines illustrate the spin states (spin up or down).

(c) For an off-diagonal operator, we ignore it and go to the next operator in the operator strings.

2. Cluster update

- (a) We generally follow two rules to construct the clusters: (1) clusters are terminated on site-operators $H_{-1,i}$ or $H_{0,i}$; and (2) the four legs of a bond operator $H_{1,b}$ ($H_{1,b'}$) belong to one cluster. Carry out this procedure until all the clusters are built, and a configuration of clusters are shown in Fig. 5.
- (b) Due to the external field breaks Z_2 symmetry, the probability of cluster update should be modified [29–31]. Clusters identified from the above rules are then flipped with probability $\frac{W_{new}}{W_{old}+W_{new}}$. Here the $W_{new/old}$ is the weight after/before cluster update.

Appendix B: $q = 3$ Potts to first order transition

As mentioned in the main text, the UUD-PM phase transition is continuous when the external magnetic is relatively small ($h < 1.5$), and the UUD-PM phase transition becomes the first order when the external magnetic is large enough ($h > 1.5$). To prove that, we plot the 3-states Binder cumulant $U(q = 3)$ as function of temperature T at different external magnetic $h = 1$, $h = 1.5$ and $h = 2$ for different system sizes $L = 6, 9, 12, 15$, as shown in Fig. 6. We notice that the $U(q = 3)$ decay smoothly at $h = 1$ for $L = 6, 9, 12, 15$, however $U(q = 3)$ begins to develop a negative dip at $h = 1.5$

for $L = 12$ and $L = 15$, which is the typical behavior close to a first-order phase transition [19, 20, 23]. When $h = 2$, the dips go to more negative, which means the first-order phase transition is more noticeable.

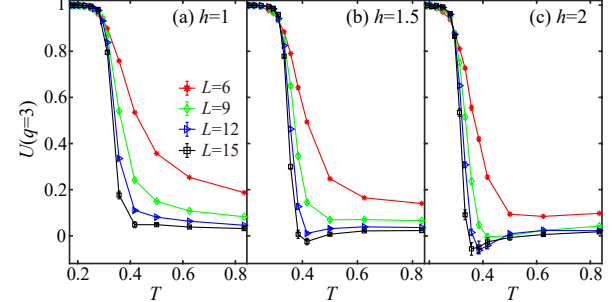


FIG. 6. Binder cumulant $U(q = 3)$ of the $q = 3$ Potts transition at (a) $h = 1$, (b) $h = 1.5$ and (c) $h = 2$.

However, we note that the negative dip in the Binder cumulant along our phase boundary has not developed into the divergence which is usually the case for the standard first order phase transition, this is consistent with the fact that the 3D $q = 3$ Potts (or its 2D quantum version in the present case at $T = 0$ from UUD to PM) is known to be a weakly first order, in fact, "almost second order" phase transition [32].

Appendix C: RG Analysis

In this section, we describe how to construct the Ginzburg-Landau theory of the 3-sublattice order parameter to the triangular lattice quantum Ising model, and analyze the phase transitions at very small external field by renormalization group (RG) methods.

1. Ginzburg-Landau Theory

To study the low-energy effective theory of the triangular lattice transverse field Ising model, we start from the formulation of the three-sublattice ordering standard Ginzburg-Landau (GL) theory. To capture physics of the three-sublattice ordered structure, the order parameter is defined at the \mathbf{K} point:

$$\psi(\mathbf{r}) = |\psi(\mathbf{r})| e^{i\theta_{\mathbf{r}}} = \sum_i m_i^z e^{i\mathbf{K} \cdot \mathbf{R}_i}, \quad (C1)$$

where $\mathbf{K} = (2\pi/3, 2\pi/3)$ is the corner of the hexagonal Brillouin zone (BZ), and \mathbf{R}_i , $i = 1, 2, 3$ represents coordinates at three sublattice sites in the unit cell at \mathbf{r} .

Traditional symmetry analysis [33–37] provides a coarse-grained order parameter field Ginzburg-Landau free energy density [37]:

$$\begin{aligned} \mathcal{F}_{ts}[\psi] = & \kappa |\nabla \psi|^2 + r |\psi|^2 + u_4 |\psi|^4 + u_6 |\psi|^6 \\ & + \lambda_6 |\psi|^6 \cos(6\theta) + \lambda_{12} |\psi|^{12} \cos(12\theta) + \dots \quad (C2) \end{aligned}$$

In the phase transitions we want to study, we expect local amplitude of the order parameter $|\psi|$ retains nonzero and slowly-variant, and the fluctuation of phase θ_r is dominant. From the following analysis, we will see why λ_{12} term is not important. These result in the further simplification of the model Eq. (C2) into

$$\mathcal{F}_{ts}[\theta_r] = \frac{1}{4\pi g}(\nabla\theta)^2 + \lambda \cos(6\theta), \quad (\text{C3})$$

where $g(T)$ is monotonously tuned by temperature T , and λ is the rescaled coupling constant of $\cos(6\theta)$ term.

From the definition of the three-sublattice order parameter, i.e. in Eq. (C1), we find when $\lambda > 0$ the phase θ falls in 6 minima that represent a six-fold degenerate clock phase, while $\lambda < 0$ represents the up-up-down (UUD) phase with nonzero net magnetization. We expect similar critical behaviors to 6-state clock model [38, 39].

A further observation [36], however, pointed out that the above three sublattice order parameter doesn't capture the physics of uniform magnetization mode, like in UUD phase, at Γ point:

$$m_r \equiv \sum_i m_i^z. \quad (\text{C4})$$

Regarding the same $S_3 \times Z_2$ symmetry as the original GL theory when the net magnetization is present, a coarse-grained Ising field, and - most importantly - a coupling between three sublattice phase mode and uniform magnetization Ising mode, are included in the model:

$$\mathcal{F}[\theta_r, m_r] = \mathcal{F}_{ts}[\theta_r] + \mathcal{F}_{\text{Ising}}[m_r] - cm_r \cos(3\theta_r). \quad (\text{C5})$$

The last term, when uniform magnetization is linearly polarized by the external uniform longitudinal field h and thus the Z_2 symmetry is broken, becomes a coupling between h and $\cos(3\theta)$. Focusing on the phase degree of freedom, the GL theory is written as:

$$\mathcal{F}[\theta_r, h] = \frac{1}{4\pi g}(\nabla\theta)^2 + \lambda \cos(6\theta) - h \cos(3\theta), \quad (\text{C6})$$

here we rescale h to absorb nonuniversal coupling coefficient, and its sign (the direction of external field) selects which 3 minima are the ground states.

2. RG Equations

The model Eq. (C3) proposed above is well-known for the existence of a power-law correlation quasi long-range ordered intermediate Berezinskii-Kosterlitz-Thouless (BKT) phase [40]:

$$\left\langle e^{i(p\theta(r)-p'\theta(0))} \right\rangle \sim r^{-p^2 g} \delta_{pp'}, \quad (\text{C7})$$

when $g(T) = \eta(T) \in (\frac{1}{9}, \frac{1}{4})$ for the triangular lattice quantum Ising model [8].

In the renormalization group (RG) language, the gradient term in Eq. (C3) is exactly marginal along the entire $\lambda = 0$ line [41–44]. The six-fold anisotropy term is relevant only when $g < \frac{1}{9}$, and symmetry-breaking long-range order is thus formed at low T ; when $g > \frac{1}{4}$ the vortex term comes in, and the vortex proliferate phase arises at high T [38]. The intermediate BKT phase is a critical phase formed by a line of central charge $c = 1$ fixed points [36], where no anisotropy is relevant and an emergent $U(1)$ symmetry is present.

The above 1st order RG analysis is performed in zero field. When nonzero uniform magnetic field is present, however, the $h \cos(3\theta)$ term is relevant everywhere $g < \frac{2}{9}$, from zero temperature to somewhere deep in disordered phase. To study how this term interacts with six-fold anisotropy term and vortex term, a detail 2nd order analysis is needed.

From the momentum shell RG, if we nondimensionalize coupling constants of every term in the theory and write it as

$$S = \int d^D x \sum_n \nu_n \Lambda^{D-\Delta_n} \phi_n(\mathbf{x}), \quad (\text{C8})$$

where D is the spatial dimension, Λ is the large-momentum cutoff, and Δ_n and ν_n is the scaling dimension and dimensionless coupling constant of operator ϕ_n , the 2nd order general RG equation involving operator product expansion (OPE) is [41]

$$\frac{d\nu_k}{dl} = (D - \Delta_k) \nu_k - \frac{S_D}{2} \sum_{nm} \nu_n \nu_m C_{nmk} + \dots = \beta(\nu_k). \quad (\text{C9})$$

Here C_{nmk} is the structure constant of OPE, and S_D is the spherical phase factor in D -dimension.

We first study the RG equations near the lower BKT critical point T_L , where $g_L \equiv g(T_L) = \frac{1}{9}$ and six-fold anisotropy term is marginal. In the $D = 2$ Kosterlitz RG we are interested here, we denote ϕ_0 the operator $(\nabla\theta)^2$, and ϕ_p the vortex operator $e^{ip\theta}$. The scaling dimensions $\Delta_0 = 2$, and $\Delta_p = \frac{p^2 g}{2}$ from Eq. (C7), resulting in the aforementioned 1st order analysis of six-fold degenerate order and relevance of external field coupling [45].

The OPE calculated by 2D free boson CFT [41, 43] tells us [46]:

$$C_{n,-n,0} = -\pi \Delta_n, \quad C_{n,m,n+m} = 1. \quad (\text{C10})$$

When only one pair of vortex operators $\phi_{\pm n}$ are in the place, only the first structure constant is nontrivial to the 2nd order. The substitution of Eq. (C10) into the general RG equation Eq. (C9) results in the well-known hyperbolic RG flows of sine-Gordon model. However, when there are more than one pair of vortex operators — exactly the case for our nonzero field theory — the coupling between constants plays an important role in determining the nature of the phase diagram.

Investigate Eq. (C6), with straightforward substitutions of nonzero coupling constants into Eq. (C9), and we write out RG equations when both $\cos(6\theta)$ and $\cos(3\theta)$ term are present in the theory:

$$\frac{d\lambda}{dl} = (2 - 18g)\lambda - \frac{\pi}{2}h^2, \quad (C11)$$

$$\frac{dh}{dl} = (2 - \frac{9}{2}g - \pi\lambda)h, \quad (C12)$$

$$\frac{dg}{dl} = -9\pi^2 g^3(4\lambda^2 + h^2) \simeq -\frac{\pi^2}{81}(4\lambda^2 + h^2). \quad (C13)$$

The above equations shows the existence of a Ising class phase transition. While the strong relevance of $h \cos(3\theta)$ term drives the parameter flow to $\lambda \rightarrow -\infty$, ie. UUD phase, in most part of the parameter space, a parameter flow starting from $\lambda \gg |h|$ when $g < g_L$ will suppress the increase of h according to Eq. (C12), thus in turn go to $\lambda \rightarrow \infty$ the clock phase. Therefore, if the system is in clock phase when temperature is low enough and no external field applied, it will undergo an Ising phase transition into UUD phase at some finite field strength when the external uniform magnetic field is turned on and increased. And $g_L, h = 0$ is a tricritical point, where clock phase, UUD phase and BKT phase boundaries merges at one point.

Here we complete the RG analysis near g_L and we now turn to study the phase transition near upper BKT temperature $g_U \equiv g(T_U) = \frac{1}{4}$. In this regime the six-fold anisotropy is no longer relevant, and the relevance of the vortex term $y \cos(\phi)$ defined on the dual lattice interacts with the external Field term. Given the complexity of duality mapping, the result is expected to be complicated. However, [38] gave a concise argument that up to the 2nd order, the coupling constants h and y don't interact:

$$\frac{dh}{dl} = (2 - \frac{9}{2}g)h, \quad (C14)$$

$$\frac{dy}{dl} = (2 - \frac{1}{2g})y, \quad (C15)$$

$$\frac{dg}{dl} = \frac{\pi^3}{g}y^2 - 9\pi^2 g^3 h^2. \quad (C16)$$

It is based on two facts: the relation when doing duality mapping between lattices:

$$9g \Leftrightarrow \frac{1}{g}, \quad y \Leftrightarrow h, \quad h \Leftrightarrow y, \quad (C17)$$

and the invariance of RG equations when $h \rightarrow -h$. If any gh or h^2 term appears in one of Eqs. (C14)-(C15), then a counterpart will also appear in the other equation, and it will break the invariance of RG equations under $h \rightarrow -h$.

Because $h \cos(3\theta)$ term is always relevant near the critical point, and the gapped disordered phase by the vortex term should be more robust to the perturbation than the gapless BKT phase, the phase boundary between UUD and disordered phase should be extrapolated directly to g_U . Therefore, the decoupled nature of multiple relevant perturbations also suggests a tricritical point at g_U and $h = 0$ [40], where BKT phase, UUD phase and disordered phase boundaries come into one point.

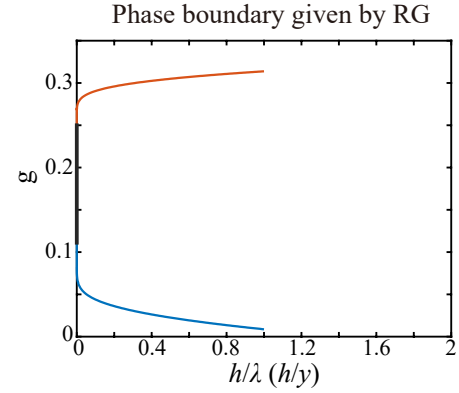


FIG. 7. The phase boundaries given from RG analysis. Here we set dimensionless $\lambda = y = 0.001$. The top orange line is where Potts phase transition occurs, and the bottom blue line is where Ising phase transition occurs.

3. Phase Diagram

To see the explicit phase transition analysis of RG at the small field regime, the best way is to show it in the phase diagram.

Here we plot the obtained RG phase diagram in Fig. 7. The parameter points in the phase diagram are the starting parameter points of RG flows. The top orange line distinguishes whether $|h|$ or y goes to unity first. The former is identified as the UUD phase, and the latter the disordered phase, and the transition between them is in 3-state Potts universal class. The bottom blue line is the boundary below which h no longer flows to unity but zero and is identified as clock phase, above which $|h|$ flows to unity faster than λ and the UUD phase is clarified here. Thus this transition is in the Ising universal class.

Appendix D: DMRG Results

As mentioned in the main text, in the ground state the system develops a clock order at field $h = 0$, which, however, is fragile under longitudinal fields. To help stabilize the order in a finite-size system and discern the subtle competition between different magnetically ordered ground states, we applied a small clock-type pinning field h_p from very small (10^{-4}) to a moderate value ($h_p = 1$) on the left boundary of the system. The calculated on-site magnetization m_z on a YC 6×30 cylinder, as shown in Fig. 8. Three-sublattice order can be clearly identified by the different colors on each site, which represents the sign of local m_z . The absolute values of m_z on sub-lattice C and A are two orders of magnitude larger than that on sub-lattice B, thus indicating a clock spin configuration. In Fig. 8(c), we see even the smallest ($h_p = 10^{-4}$) field can induce a clock order, and the latter is converged to about 0.43 for $h_p \geq 10^{-2}$. Besides, in Fig. 8(b) we observe that e_g quickly converges as the pinning field h_p increases, and the energy result e_g has converged to six digits for $h_p > 0.1$.

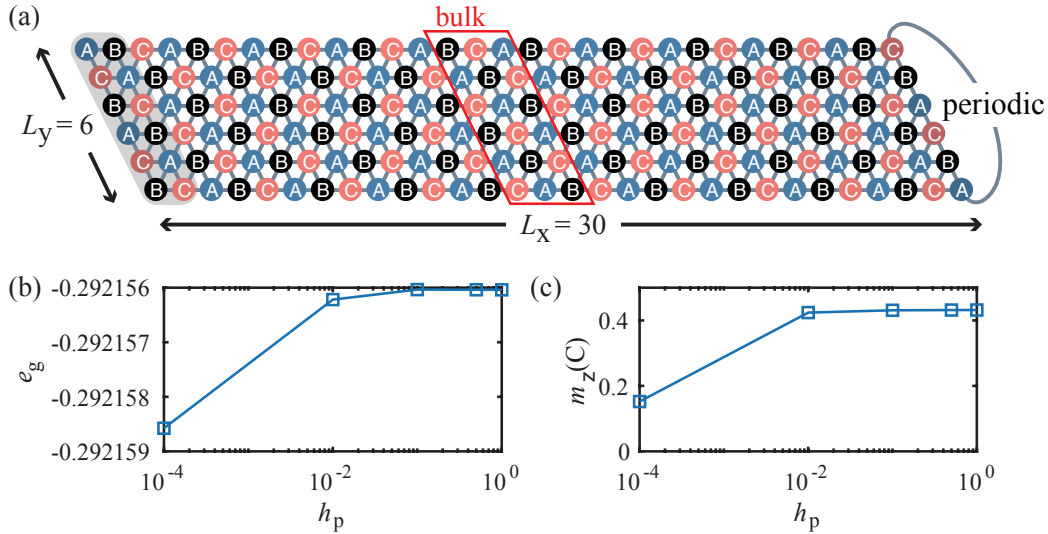


FIG. 8. (a) Illustration of the three-sublattice spin structure on the YC6×30 cylinder in the clock order phase, with the parameters $J_1 = 1$, $J_2 = 0$, $\Delta = 0.2$, $h = 0$ and the clock-type field $h_p = 10^{-4}$ pinning on the left two columns of the system (the gray area). The red and blue color represent spin up ($m_z > 0$) and spin down ($m_z < 0$) along the magnetic easy axis, and the black one stands for the superposition of spin up and down with zero net z -component ($m_z \simeq 0$). The brightness of the color represents the absolute strength of local magnetization. (b) shows the bulk energy u_b vs pinning field h_p , and (c) shows the bulk magnetization m_z on the sub-lattice C. The bulk sites involved in the calculations are indicated in (a) within the red parallelogram.

Therefore, in the main text we fix the pinning field $h_p = 1$ and

perform the calculations at low magnetic fields as shown in Fig. 4(a) of the main text.

[1] F. A. Cevallos, K. Stolze, T. Kong, and R. J. Cava, *Mater. Res. Bull.* **105**, 154 (2018).

[2] Y. Shen, C. Liu, Y. Qin, S. Shen, Y.-D. Li, R. Bewley, A. Schneidewind, G. Chen, and J. Zhao, *Nat. Commun.* **10**, 4530 (2019).

[3] Y. Li, S. Bachus, H. Deng, W. Schmidt, H. Thoma, V. Hutaniu, Y. Tokiwa, A. A. Tsirlin, and P. Gegenwart, *Phys. Rev. X* **10**, 011007 (2020).

[4] Z. Hu, Z. Ma, Y.-D. Liao, H. Li, C. Ma, Y. Cui, Y. Shangguan, Z. Huang, Y. Qi, W. Li, Z. Y. Meng, J. Wen, and W. Yu, *Nature Communications* **11**, 5631 (2020).

[5] H. Li, Y. D. Liao, B.-B. Chen, X.-T. Zeng, X.-L. Sheng, Y. Qi, Z. Y. Meng, and W. Li, *Nat. Commun.* **11**, 1111 (2020).

[6] C. Liu, C.-J. Huang, and G. Chen, *Phys. Rev. Research* **2**, 043013 (2020).

[7] R. Moessner and S. L. Sondhi, *Phys. Rev. Lett.* **86**, 1881 (2001).

[8] S. V. Isakov and R. Moessner, *Phys. Rev. B* **68**, 104409 (2003).

[9] Y.-C. Wang, Y. Qi, S. Chen, and Z. Y. Meng, *Phys. Rev. B* **96**, 115160 (2017).

[10] Z. Dun, M. Daum, R. Baral, H. E. Fischer, H. Cao, Y. Liu, M. B. Stone, J. A. Rodriguez-Rivera, E. S. Choi, Q. Huang, H. Zhou, M. Mourigal, and B. Frandsen, Neutron scattering investigation of proposed kosterlitz-thouless transitions in the triangular-lattice ising antiferromagnet tmmgao4 (2020), arXiv:2011.00541 [cond-mat.str-el].

[11] Y. Qin, Y. Shen, C. Liu, H. Wo, Y. Gao, Y. Feng, X. Zhang, G. Ding, Y. Gu, Q. Wang, S. Shen, H. C. Walker, R. Bewley, J. Xu, M. Boehm, P. Steffens, S. Ohira-Kawamura, N. Muraia, A. Schneidewind, X. Tong, G. Chen, and J. Zhao, Field-tuned quantum effects in a triangular-lattice ising magnet (2020), arXiv:2011.09376 [cond-mat.str-el].

[12] C.-J. Huang, X. Wang, Z. Wang, and G. Chen, Emergent halperin-saslow mode and gauge glass in quantum ising magnet tmmgao4 (2020), arXiv:2011.05919 [cond-mat.str-el].

[13] Z. Zhou, D.-X. Liu, Z. Yan, Y. Chen, and X.-F. Zhang, arXiv e-prints , arXiv:2005.11133 (2020), arXiv:2005.11133 [cond-mat.str-el].

[14] Z. Zhou, C.-L. Liu, Z. Yan, Y. Chen, and X.-F. Zhang, arXiv e-prints , arXiv:2010.01750 (2020), arXiv:2010.01750 [cond-mat.str-el].

[15] A. W. Sandvik, *AIP Conference Proceedings* **1297**, 135 (2010).

[16] A. W. Sandvik, *Physical Review E* **68**, 056701 (2003).

[17] R. G. Melko, in *Strongly Correlated Systems* (Springer, 2013) pp. 185–206.

[18] J. Zhao, Z. Yan, M. Cheng, and Z. Y. Meng, arXiv e-prints , arXiv:2011.12543 (2020), arXiv:2011.12543 [cond-mat.str-el].

[19] Y. Kato and T. Misawa, *Phys. Rev. B* **92**, 174419 (2015).

[20] Y. Liu, Z. Y. Meng, and S. Yin, *Phys. Rev. B* **103**, 075147 (2021).

[21] K. Binder, *Phys. Rev. Lett.* **47**, 693 (1981).

[22] K. Binder, *Z. Phys. B* **43**, 119 (1981).

[23] K. Binder and D. P. Landau, *Phys. Rev. B* **30**, 1477 (1984).

[24] R. Samajdar, W. W. Ho, H. Pichler, M. D. Lukin, and S. Sachdev, *Proceedings of the National Academy of Sciences* **118**, 10.1073/pnas.2015785118 (2021).

[25] S. Ebadi, T. T. Wang, H. Levine, A. Keesling, G. Semeghini, A. Omran, D. Bluvstein, R. Samajdar, H. Pichler, W. W. Ho, S. Choi, S. Sachdev, M. Greiner, V. Vuletic, and M. D. Lukin, arXiv e-prints , arXiv:2012.12281 (2020), arXiv:2012.12281 [quant-ph].

- [26] P. Scholl, M. Schuler, H. J. Williams, A. A. Eberharter, D. Barredo, K.-N. Schymik, V. Lienhard, L.-P. Henry, T. C. Lang, T. Lahaye, A. M. Läuchli, and A. Browaeys, Programmable quantum simulation of 2d antiferromagnets with hundreds of rydberg atoms (2020), [arXiv:2012.12268 \[quant-ph\]](https://arxiv.org/abs/2012.12268).
- [27] A. D. King, J. Carrasquilla, J. Raymond, I. Ozfidan, E. Andriyash, A. Berkley, M. Reis, T. Lanting, R. Harris, F. Altomare, K. Boothby, P. I. Bunyk, C. Enderud, A. Fréchette, E. Hoskinson, N. Ladizinsky, T. Oh, G. Poulin-Lamarre, C. Rich, Y. Sato, A. Y. Smirnov, L. J. Swenson, M. H. Volkmann, J. Whittaker, J. Yao, E. Ladizinsky, M. W. Johnson, J. Hilton, and M. H. Amin, *Nature* **560**, 456 (2018).
- [28] A. D. King, J. Raymond, T. Lanting, S. V. Isakov, M. Mohseni, G. Poulin-Lamarre, S. Ejtemaei, W. Bernoudy, I. Ozfidan, A. Y. Smirnov, M. Reis, F. Altomare, M. Babcock, C. Baron, A. J. Berkley, K. Boothby, P. I. Bunyk, H. Christiani, C. Enderud, B. Evert, R. Harris, E. Hoskinson, S. Huang, K. Jooya, A. Khodabandou, N. Ladizinsky, R. Li, P. A. Lott, A. J. R. MacDonald, D. Marsden, G. Marsden, T. Medina, R. Molavi, R. Neufeld, M. Norouzpour, T. Oh, I. Pavlov, I. Perminov, T. Prescott, C. Rich, Y. Sato, B. Sheldon, G. Sterling, L. J. Swenson, N. Tsai, M. H. Volkmann, J. D. Whittaker, W. Wilkinson, J. Yao, H. Neven, J. P. Hilton, E. Ladizinsky, M. W. Johnson, and M. H. Amin, arXiv e-prints , arXiv:1911.03446 (2019), [arXiv:1911.03446 \[quant-ph\]](https://arxiv.org/abs/1911.03446).
- [29] O. F. Syljuåsen and A. W. Sandvik, *Physical Review E* **66**, 046701 (2002).
- [30] Z. Yan, Y. Wu, C. Liu, O. F. Syljuåsen, J. Lou, and Y. Chen, *Physical Review B* **99**, 165135 (2019).
- [31] Z. Yan, [arXiv preprint arXiv:2011.08457](https://arxiv.org/abs/2011.08457) (2020).
- [32] H. W. J. Blöte and R. H. Swendsen, *Phys. Rev. Lett.* **43**, 799 (1979).
- [33] E. Domany, M. Schick, J. S. Walker, and R. B. Griffiths, *Phys. Rev. B* **18**, 2209 (1978).
- [34] E. Domany and M. Schick, *Phys. Rev. B* **20**, 3828 (1979).
- [35] S. Alexander, *Physics Letters A* **54**, 353 (1975).
- [36] K. Damle, *Phys. Rev. Lett.* **115**, 127204 (2015).
- [37] S. Biswas and K. Damle, *Phys. Rev. B* **97**, 085114 (2018).
- [38] J. V. José, L. P. Kadanoff, S. Kirkpatrick, and D. R. Nelson, *Physical Review B* **16**, 1217 (1977).
- [39] M. S. S. Challa and D. P. Landau, *Phys. Rev. B* **33**, 437 (1986).
- [40] S. Sachdev, *Quantum Phase Transitions*, 2nd ed. (Cambridge University Press, Cambridge, 2011).
- [41] E. Fradkin, *Field theories of condensed matter physics* (Cambridge University Press, 2013) Book 4, pp. 63–89.
- [42] N. Nagaosa, *Quantum field theory in strongly correlated electronic systems* (Springer Science & Business Media, 1999).
- [43] P. Francesco, P. Mathieu, and D. Sénéchal, *Conformal field theory* (Springer Science & Business Media, 2012).
- [44] M. Henkel, *Conformal invariance and critical phenomena* (Springer Science & Business Media, 2013).
- [45] $h \rightarrow h\Lambda^{3/2}$ makes h a dimensionless quantity so that it is comparable with unity, and all other terms are already marginal.
- [46] The second structure constant is valid only when $n, m \neq 0$, for only vortex operator calculation involved.